
A Model-based Deep Learning Reconstruction for X-ray CT

Kaichao Liang, Li Zhang, Yirong Yang, Hongkai Yang, Yuxiang Xing *
Key Laboratory of Particle & Radiation Imaging, Tsinghua University
Beijing, China 100084

*Corresponding author: Yuxiang Xing Email: xingyx@mail.tsinghua.edu.cn

Abstract

Low dose CT is of great interest in these days. Dose reduction raises noise level in projections and decrease image quality in reconstructions. Model based image reconstruction can combine statistical noise model together with prior knowledge into an Bayesian optimization problem so that significantly reduce noise and artefacts. In this work, we propose a model-base deep learning for CT reconstruction so that a reconstruction network can be trained with no ground-truth images needed. Instead of minimizing cost function for each image, the network learns to minimize an ensemble cost function for the whole training set. No iteration will be needed for real data reconstruction using such a trained network. We experimented with a penalized weighted least-squares (PWLS) cost function for low dose CT reconstruction and tested on data from a practical dental CT. Very encouraging results with great noise reductions are obtained.

1 Introduction

As X-ray CT is a widely used medical imaging modality for clinical diagnosis tool, its radiation dose is of big concerned. High level of dose received by patients increase the risk of cancer [1]. In the past decades, lowering X-ray dose by adjusting tube-voltage or tube-current-time have been studied extensively [2, 3, 4]. However, further reducing incident photons can cause high level statistical noise, and electronic noise becomes non-neglectable as well. If directly reconstructed with an FBP type algorithm, the noise in projection data will be magnified by the high-pass filtration (RL filter or SL filter) and degrade image quality.

Previously, many researches have been conducted on low dose CT (LDCT) image optimization[1]. These algorithms generally can be divided into three categories. The first category is filtration method. Manually designed filters or filtration algorithms are adopted to suspense noise. Pre-processing methods focus on projection domain denoising [5], and post-processing methods focus on image domain denoising after analytical reconstruction [6]. Zhang et al. proposed a LDCT local texture restoration algorithm with priors extracted from NDCT image dataset [7], which integrated NDCT reference dataset into filtration methods. However, low-pass filters restrain noise but generally cause detail information loss in projection data which further cause image blurring. The second category is iterative reconstruction methods [8, 9, 10]. Model-based iterative reconstruction (MBIR) is based on Bayesian theory and models noise model, physical process and system configuration into reconstruction. For example, combining statistical iterative reconstruction (SIR) with none-local-mean (NLM) constraint for low-dose CT reconstruction [8, 9] to suppress noise. Instead of using NLM, Xu adopted dictionary learning which learns prior constraint based on normal-dose CT dataset [10]. The images reconstructed from low-dose projections are expected to be of similar distribution as normal dose CT reconstructions. However, iterative

process is very time consuming which is obstructed its usage in real-time reconstruction. Besides, hyper-parameters in cost function and number of iteration need to be tuned according to different data.

Recently, deep learning methods have been widely conducted in LDCT problems [11, 12, 13, 14]. Hu and his colleagues used a three-layer CNN structure for LDCT image optimization and achieved visible image quality improvements [11]. Later, Chen proposed a more complex encoder-decoder structure CNN for LDCT and achieved better results [12]. Convolutional neural networks (CNN) learns the relationship between LDCT images and NDCT images from training set. Because of the large cost of real data, LDCT and corresponding NDCT images are often from simulations. In these works, normal dose CT (NDCT) images are required to form labels, which is easy to access in simulation study. However, in practical complex situation, features of real data can be very different from simulation, which could heavily influences the generalization of networks. No ground-truth images available for labels in real situation become an obstacle for practical problems.

In this work, we propose a model based deep learning (MBDL) method for CT reconstruction that requires no ground-truth information. The network can be directly trained with LDCT projection data only, encouraging reconstruction results from practical low dose dental CT data are obtained.

2 Methods

2.1 Cost function to model X-ray CT imaging

In regression problem, labels are usually used to form L1/L2-norm as the cost function of networks to minimize. In many situations, ground-truth information might be available. The basic idea of our method is to incorporate a system model based cost function for deep-learning network. Without losing the generality, we took Bayesian estimation principle to construct our cost function for CT reconstruction similar to MBIR methods. In general, Bayesian cost function contains two terms: data fidelity term which models the noise of projection data, and prior term which constraint the reconstructed image to follow prior information about general image characteristics.

$$\Phi(\boldsymbol{\mu}) = \phi_f(\boldsymbol{\mu}, \mathbf{p}, \mathbf{H}) + \lambda\phi_p(\boldsymbol{\mu}) \quad (1)$$

Here, Φ denotes a general Bayesian cost function with ϕ_f the data fidelity term and ϕ_p the priors. Here, \mathbf{p} is the a CT projection data that is very noisy from a low dose scan, and \mathbf{H} the system matrix of CT, $\boldsymbol{\mu}$ denotes the estimation of linear attenuation map, i.e. be the output of network. The hyper-paramete λ in Eq.1 is commonly used to adjust the strength of two terms. Hence, with known imaging system matrix and projection data, the cost function avoids using any ground-truth label and model imaging physics instead.

In X-ray CT imaging, the data are generally modelled to be bin-to-bin independent Poisson or Compound Poisson distributed[15]. After negative log operation of Poisson distributed data, a sinogram projection is approximately Gaussian with its variance dependent on mean [16]. Thus, we have the likelihood to be:

$$\mathbf{P}(\mathbf{p}; \boldsymbol{\mu}) = \exp(-(\mathbf{H}\boldsymbol{\mu} - \mathbf{p})^T \boldsymbol{\Sigma}^{-1} (\mathbf{H}\boldsymbol{\mu} - \mathbf{p})) \quad (2)$$

Here, $\boldsymbol{\Sigma}^{-1}$ is a diagonal matrix and its diagonal elements denote the variance of projections. Various priors have been studied in X-ray CT reconstruction [9, 10, 17, 18, 19]. In this work, we adopt a constraint derived from none local mean (NLM) [8]. The NLM term can be formulated as:

$$\phi_{\text{NLM}}(\boldsymbol{\mu}) = \frac{1}{2} \sum_i \sum_{i' \in \mathcal{N}(i)} W_{ii'} (\mu_i - \mu_{i'})^2 \quad (3)$$

Here, $\mathcal{N}(i)$ denotes the neighboring pixels of i within a searching window and $W_{ii'}$ denotes the weight of similarity computed from:

$$W_{ii'} = \frac{\exp(-\|\Pi(\mu_i) - \Pi(\mu_{i'})\|_{2,a}^2/h)}{\sum_{j \in \mathcal{N}(i)} \exp(-\|\Pi(\mu_i) - \Pi(\mu_j)\|_{2,a}^2/h)} \quad (4)$$

With $\Pi(\cdot)$ being a patch extractor, $\|\cdot\|_{2,a}$ the L2-norm with a Gaussian kernel a to weight the distance in a patch and a normalization parameter. If neighboring patches of two pixels are similar,

the two pixels are likely to be the same kind of materials and gets a high weight. In this way, NLM can preserve structures well while restrain noise. Combining Eq. 2 and 3, we obtain a Bayesian cost function which falls into the category of penalized weighted least square (PWLS). It is used to guide our deep learning network:

$$\Phi(\boldsymbol{\mu}) = (\mathbf{p} - \mathbf{H}\boldsymbol{\mu})^T \boldsymbol{\Sigma}^{-1} (\mathbf{p} - \mathbf{H}\boldsymbol{\mu}) + \lambda \phi_{\text{NLM}}(\boldsymbol{\mu}) \quad (5)$$

2.2 Network architecture and training

To enforce the cost function as in Eq.5, we constructed a reconstruction network as displayed in Fig. 1. It takes noisy projection data as inputs and output reconstructed images at the end. The network is consisted of three blocks to do dual-domain learning similar to our previous work [20, 21].

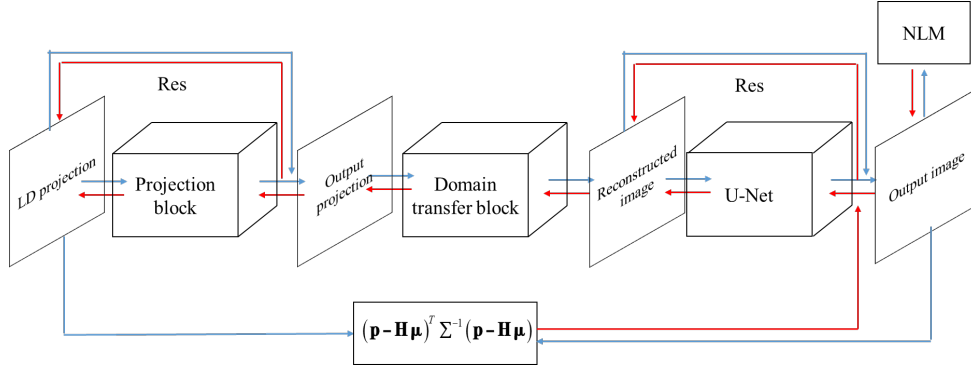


Figure 1: Architecture of model-based deep learning network for CT reconstruction.

First, projection block reduces the noise in projection domain. Projection block contains five convolutional layers. Each convolutional layer is followed with leaky-Relu activation function. Next, domain transfer block is an analytical inverse operator. We adopt the matrix format of FBP reconstruction as Eq.6

$$\boldsymbol{\mu} = \mathbf{H}_W^T \mathbf{F} (\mathbf{W} \cdot \mathbf{p}) \quad (6)$$

Here, \mathbf{W} denotes projection weighting matrix, it weights the projection. \mathbf{F} is a matrix form of RL filtration, it filters the projection data along the detector axis. \mathbf{H}_W^T denotes the operator of weighted back-projection. All the matrix in the reconstruction block is pre-calculated and not trained in this study, but gradients can path through the reconstruction block from image domain back to projection domain, which is critical in our network. Following reconstruction block, an image domain U-Net [22] refines the reconstruction results and output the final estimation. The U-Net structure achieves big receptive-field with pooling layers, while it recovers local spatial resolution by combining up-sampled features with un-pooled features. Both image domain network and projection domain network adopt residual structure to ease the network training process.

In our training, the network parameters are updated to minimize the Bayesian cost function over the whole training set.

$$v_1, \dots, v_M = \underset{v_1, \dots, v_M}{\operatorname{argmin}} \sum_{k \in 1:K} \Phi(\boldsymbol{\mu}^k) \quad (7)$$

Here, k indexes the attenuation map in the training dataset of size K , and $v_1, \dots, v_m, \dots, v_M$ denote the parameters in the network.

For each training step, gradients of cost function with respect to k^{th} output image can be calculated from Eq. 5 as:

$$\frac{\partial \Phi(\boldsymbol{\mu}^k)}{\partial \mu_i^k} = \left[\mathbf{H}^T (\mathbf{H}\boldsymbol{\mu}^k - \mathbf{p}) \right]_i \boldsymbol{\Sigma}_i^{-1} + \lambda \sum_{i' \in \mathcal{N}(i)} W_{ii'} (\mu_i^k - \mu_{i'}^k) \quad (8)$$

Here, subscript i denotes the i^{th} element of a vector. Further, the gradients of the cost function with respect to network parameters can be calculated by chain rule:

$$\frac{\partial \Phi(\boldsymbol{\mu}^k)}{\partial v_m^n} = \sum_i \frac{\partial \Phi(\boldsymbol{\mu}^k)}{\partial \mu_i^k} \cdot \frac{\partial \mu_i^k}{\partial v_m^n} \quad (9)$$

with n indexing the n^{th} training iteration.

Parameters are updated with standard gradient descent method to minimize the cost function:

$$v_m^{n+1} = v_m^n - \alpha \sum_{k \in 1:K} \frac{\partial \Phi(\boldsymbol{\mu}^k)}{\partial v_m^n} \quad (10)$$

Here, α denotes the learning rate. Other optimization method can also be used to replace the gradient descending method. It is worth to emphasize that we train the network by directly updating parameters of network as above.

Different from supervised pixel-to-pixel loss, Bayesian cost function does not provide clear optimization direction in image domain for output images. To be more specific, the gradients of output image do not force output image with a clear goal in image domain in different training steps, which makes the network converges slowly in training. Thus, we applied some tricks to accelerate training process. In the early epochs, we train each data in training set for several times continuously, then change to another training data. Training each data continuously help network to catch more robust rule from Bayesian cost function. Moreover, in the early epochs, we only train the network with data fidelity term so that the main structure of reconstructed images can be learned efficiently. After the pre-training process, prior constrain is added.

3 Experiments and results

3.1 Study with simulated projection data

We first carried out our experiments on 3872 practical high quality dental CT images. We simulated the LDCT projections as network inputs. Among them, 3400 randomly chosen simulated projection data were used as training set while the left projections and the corresponding high-quality images formed test set. The high-quality dental CT images were not available to training process but only used as ground-truth for performance evaluation of the reconstruction results during inference, thus the results can be evaluated both in vision and quantitatively. Both ground-truth images and reconstruction images were 640^2 with pixel size 0.25mm. The projections were of uniformly distributed 720 fan-beam views over 2π , and 640 detector bins with bin size 0.512mm. The projections were simulated with ray-tracing forward projection method and Poisson noise was added with 5000 incident photons.

In Fig.2, ground-truth, LDCT FBP reconstruction, NLM-WLS iterative reconstruction, and MBDL network reconstruction were displayed for visual comparison. Details denoted by red boxes were zoomed-in and displayed in the lower left corner. As shown in Fig.2, the noise was well suppressed in both iterative reconstruction and MBDL reconstruction, the details of teeth and bone were restored to a large extent as in zoomed-in.

For further quantitative analysis, we compared different LDCT reconstruction results with ground-truth images by calculating mean RRMSE and SSIM indexes based on 25 randomly chosen test images:

$$\text{RRMSE}(\hat{\boldsymbol{\mu}}, \boldsymbol{\mu}) = \frac{\|\hat{\boldsymbol{\mu}} - \boldsymbol{\mu}\|_2}{\|\boldsymbol{\mu}\|_2} \quad (11)$$

$$\text{SSIM}(\hat{\boldsymbol{\mu}}, \boldsymbol{\mu}) = \frac{(2\hat{\boldsymbol{\mu}}\boldsymbol{\mu} + C_1)(2\sigma_{\hat{\boldsymbol{\mu}}, \boldsymbol{\mu}}^2 + C_2)}{(\hat{\boldsymbol{\mu}}^2 + \boldsymbol{\mu}^2 + C_1)(\sigma_{\hat{\boldsymbol{\mu}}}^2 + \sigma_{\boldsymbol{\mu}^2}^2 + C_2)} \quad (12)$$

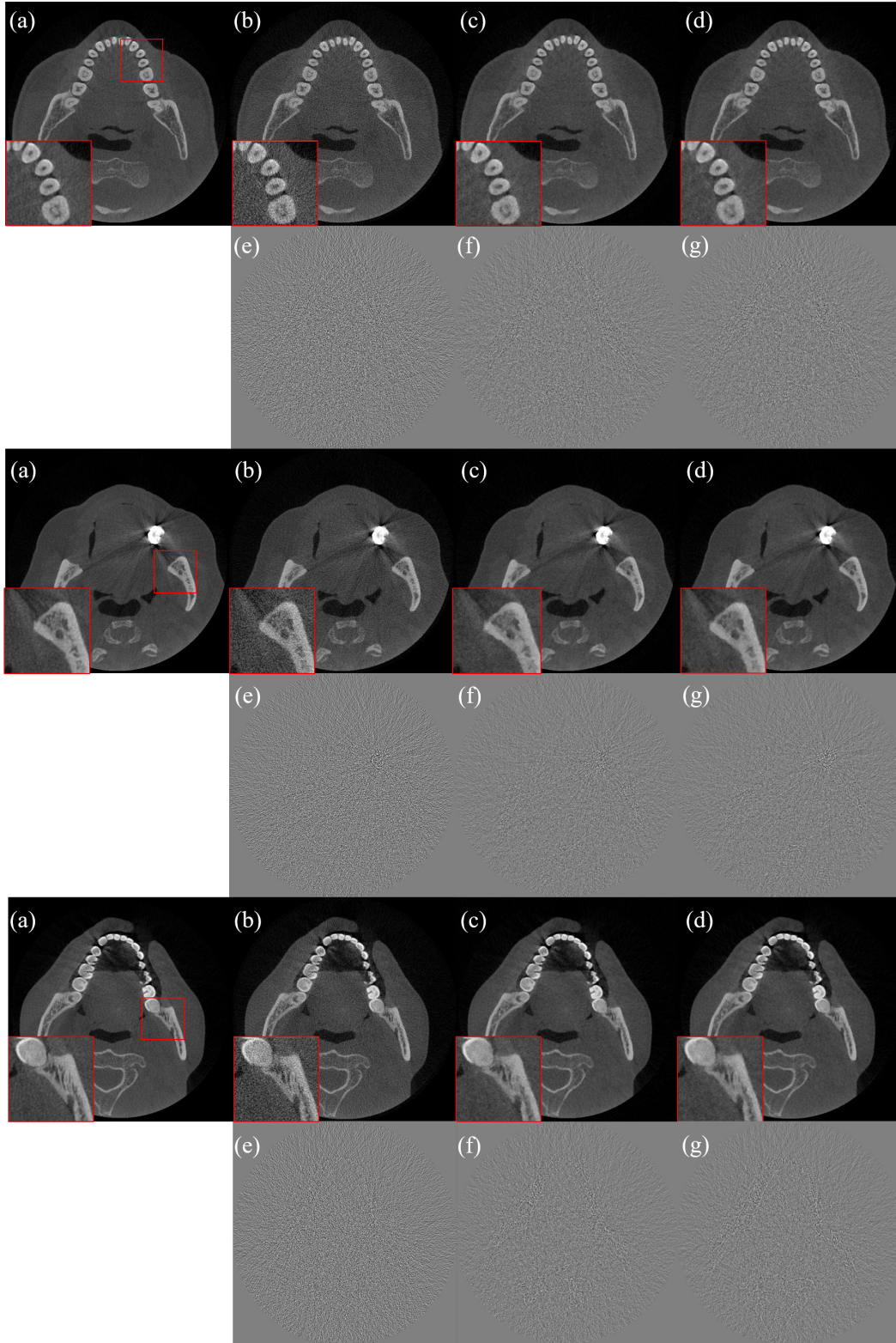


Figure 2: Comparison of different reconstruction methods. (a): Ground-truth, (b): LDCT FBP, (c): NLM-WLS iterative reconstruction, (d): LDCT MBDL reconstruction, (e): Residual map between (a) and (b), (f): Residual map between (a) and (c), (g): Residual map between (a) and (d).

Here, $\hat{\mu}$ denotes LDCT reconstruction results of different methods to be evaluated, and μ corresponding ground-truth. C_1, C_2 are constants. The mean and standard deviation of RRMSE and SSIM indexes between different FBP reconstruction methods and ground-truth were compared in Tab.1. Both WLS-NLM iterative reconstruction and MBDL reconstruction significantly reduce the RRMSE and improve SSIM indexes from LDCT FBP reconstruction results, while the MBDL reconstructions achieved slightly better quantitative performance than WLS-NLM iterative reconstructions in practice.

Table 1: RRMSE and SSIM between ground-truth and LDCT reconstruction

Method	LDCT FBP	LDCT WLS+NLM IR	LDCT MBDL
RRMSE	0.2560±0.0094	0.1164±0.0022	0.1082±0.0039
SSIM	0.9394±0.0083	0.9868±0.0015	0.9885±0.0015

3.2 Reconstruction of practical raw data with additional simulated noise

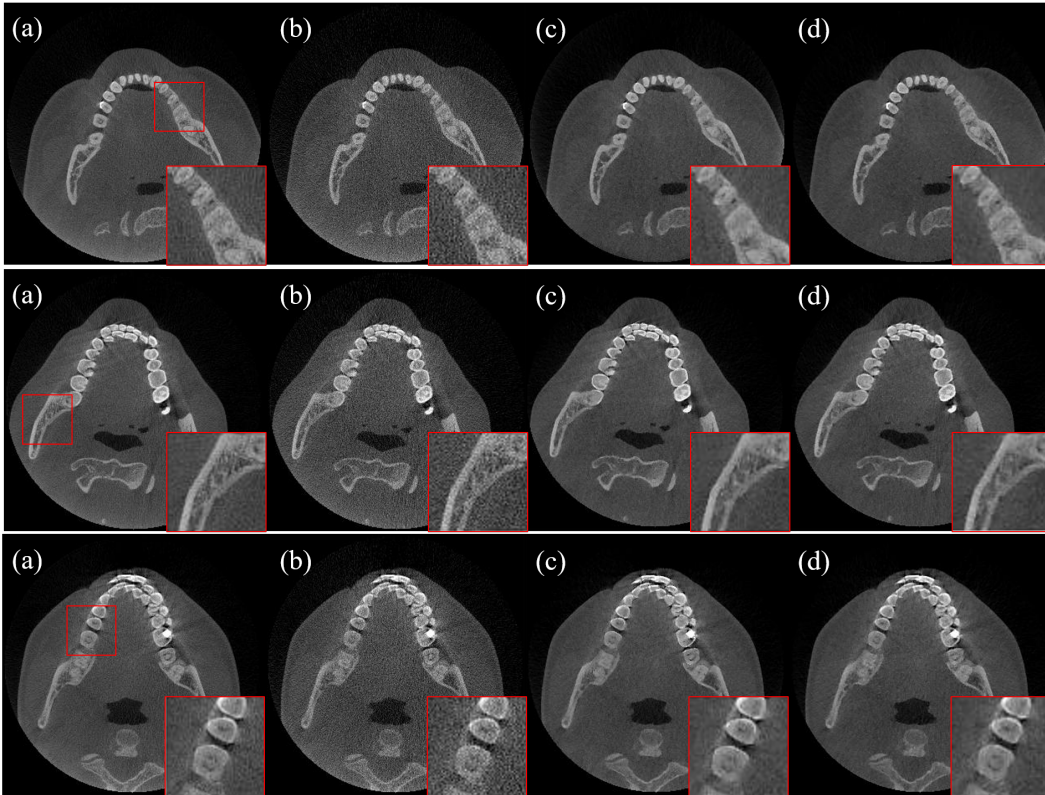


Figure 3: Comparison of different reconstruction methods. (a): NDCT Hanning + FBP, (b): LDCT Hanning + FBP, (c): NLM-WLS iterative reconstruction, (d): LDCT MBDL reconstruction.

We further carried out our experiments on practical dental CT raw data while manually increasing the noise level by additional Poisson noise, thus the situation is close to reality LDCT. In total, raw data from 3872 patients were collected. Among them, randomly chosen 3400 data were used as training set with the others forming test set for the proposed network reconstruction method. The projections were of uniformly distributed 600 fan-beam views over 2π , and 656 detector bins covering half of the ROI (reduced size detector) [23]. The size of detector bins was 0.25mm. To simulate low dose situation, original normal-dose projection data (no image domain ground truth) were treated as noise-free reference data, Poisson noise was added with 5000 incident photons. Reconstruction images were 360^2 with pixel size 0.5mm.

In Fig.3, FBP reconstruction of NDCT with Hanning filter, LDCT FBP reconstruction with Hanning filter, NLM-WLS iterative reconstruction, and MBDL network reconstruction were displayed for visual comparison. We applied a 5-order Hanning window filtration in FBP reconstructions for noise reduction in this comparison. Details denoted by red arrow were zoomed-in and displayed in the lower right corner. Similar with full-simulation cases, both iterative reconstruction and MBDL network reconstruction suppressed the noise and restored rich structures of teeth. The two algorithms achieved similar visual results.

4 Conclusion

In this work, we proposed a model-based deep learning reconstruction for LDCT. The proposed method adopt a Bayesian cost function and construct a dual-domain network allowing easy error propagation for the cost function minimization. The MBDL network is trained to minimize the cost function for the whole dataset with no ground-truth information needed. After training, the network can complete reconstruction without time-consuming iterative steps and reduced noise in a level comparable to iterative methods. Fundamentally, the proposed method integrates the optimization principle of iterative reconstruction methods with deep learning. This method can be easily extended to other scan modality and geometry with constraints or various combination of regularizations for problems such as sparse-view and limited-angle CT reconstruction.

References

- [1] E J Hall and D J Brenner. Cancer risks from diagnostic radiology. *British Journal of Radiology*, 81(965):362–378, 2008.
- [2] D P Naidich, C H Marshall, . Gribbin, C., R S Arams, and D I Mccauley. Low-dose ct of the lungs: preliminary observations. *Radiology*, 175(3):729, 1990.
- [3] Funama Yoshinori, Awai Kazuo, Miyazaki Osamu, Nakayama Yoshiharu, Goto Taiga, Omi Yasuo, Shimonobo Toshiaki, Liu Duo, Yamashita Yasuyuki, and Hori Shinichi. Improvement of low-contrast detectability in low-dose hepatic multidetector computed tomography using a novel adaptive filter: evaluation with a computer-simulated liver including tumors. *Investigative Radiology*, 41(1):1–7, 2006.
- [4] Funama Yoshinori, Awai Kazuo, Nakayama Yoshiharu, and et.al. Radiation dose reduction without degradation of low-contrast detectability at abdominal multisection ct with a low-tube voltage technique: phantom study. *Radiology*, 237:905–910, 2005.
- [5] Wang Jing, Hongbing Lu, Tianfang Li, and Zhengrong Liang. Sinogram noise reduction for low-dose ct by statistics-based nonlinear filters. In *Medical Imaging: Image Processing*, 2005.
- [6] Anja Borsdorf, Steffen Kappler, Rainer Raupach, Frederic Noo, and Joachim Hornegger. Local orientation-dependent noise propagation for anisotropic denoising of ct-images. In *Nuclear Science Symposium Conference Record*, 2010.
- [7] Y. Zhang, J. Rong, H. Lu, Y. Xing, and J. Meng. Low-dose lung ct image restoration using adaptive prior features from full-dose training database. *IEEE Trans Med Imaging*, 36(12):2510–2623, 2017.
- [8] Zhang Hao, Jianhua Ma, Wang Jing, Liu Yan, and Zhengrong Liang. Adaptive nonlocal means-based regularization for statistical image reconstruction of low-dose x-ray ct. In *Medical Imaging: Physics of Medical Imaging*, 2015.
- [9] Hao Zhang, Jianhua Ma, Jing Wang, Yan Liu, Hongbing Lu, and Zhengrong Liang. Statistical image reconstruction for low-dose ct using nonlocal means-based regularization. *Computerized Medical Imaging & Graphics*, 38(6):423–435, 2014.
- [10] Xu Qiong, Yu Hengyong, Mou Xuanqin, Zhang Lei, Hsieh Jiang, and Wang Ge. Low-dose x-ray ct reconstruction via dictionary learning. *IEEE Transactions on Medical Imaging*, 31(9):1682–1697, 2012.
- [11] Ge Wang, Hu Chen, Jiliu Zhou, Ke Li, Peixi Liao, Weihua Zhang, and Yi Zhang. Low-dose ct via convolutional neural network. *Biomedical Optics Express*, 8(2):679, 2017.
- [12] H. Chen, Y. Zhang, M. K. Kalra, F. Lin, Y. Chen, P. Liao, J. Zhou, and G. Wang. Low-dose ct with a residual encoder-decoder convolutional neural network (red-cnn). *IEEE Trans Med Imaging*, PP(99):2524–2535, 2017.
- [13] C. Zhang and Y. Xing. Ct artifact reduction via u-net cnn. In *Society of Photo-optical Instrumentation Engineers*, 2018.
- [14] Q. Yang, P. Yan, Y. Zhang, H. Yu, Y. Shi, X. Mou, M. K. Kalra, Y. Zhang, L. Sun, and G. Wang. Low-dose ct image denoising using a generative adversarial network with wasserstein distance and perceptual loss. *IEEE Transactions on Medical Imaging*, 37(6):1348–1357, 2017.
- [15] Idris A. Elbakri and Jeffrey A. Fessler. Efficient and accurate likelihood for iterative image reconstruction in x-ray computed tomography. *Proc Spie*, 5032, 2003.
- [16] J Wang, Z Lu, Hliang, D Eremina, G Zhang, S Wang, J Chen, and J Manzione. An experimental study on the noise properties of x-ray ct sinogram data in radon space. *Physics in Medicine & Biology*, 53(12):3327–3341, 2008.
- [17] Ritschl Ludwig, Bergner Frank, Fleischmann Christof, and Kachelriess Marc. Improved total variation-based ct image reconstruction applied to clinical data. *Physics in Medicine & Biology*, 56(6):1545–1561, 2011.
- [18] Kim Kyungsang, Ye Jong Chul, Worstell William, Ouyang Jinsong, Rakvongthai Yothin, El Fakhri Georges, and Li Quanzheng. Sparse-view spectral ct reconstruction using spectral patch-based low-rank penalty. *IEEE Transactions on Medical Imaging*, 34(3):748–760, 2015.

- [19] Ruoqiao Zhang, Hye Ye Dong, Debashish Pal, Jean Baptiste Thibault, and Charles A. Bouman. A gaussian mixture mrf for model-based iterative reconstruction with applications to low-dose x-ray ct. *IEEE Transactions on Computational Imaging*, 2(3):359–374, 2016.
- [20] Kaichao Liang, Hongkai Yang, and Yuxiang Xing. Comparison of projection domain, image domain, and comprehensive deep learning for sparse-view x-ray ct image reconstruction. *Arxiv 1804.04289*, 2018.
- [21] Hong Kai Yang, Kai Chao Liang, Ke Jun Kang, and Yu Xiang Xing. Slice-wise reconstruction for low-dose cone-beam ct using a deep residual convolutional neural network. *Nuclear Science and Engineering*, 30(4):53–61, 2019.
- [22] Olaf Ronneberger, Philipp Fischer, and Thomas Brox. U-net: Convolutional networks for biomedical image segmentation. In *International Conference on Medical Image Computing & Computer-assisted Intervention*, 2015.
- [23] Liang Li, Zhiqiang Chen, Li Zhang, Yuxiang Xing, and Kejun Kang. A cone-beam tomography system with a reduced size planar detector: A backprojection-filtration reconstruction algorithm as well as numerical and practical experiments. *Applied Radiation & Isotopes Including Data Instrumentation & Methods for Use in Agriculture Industry & Medicine*, 65(9):1041–1047, 2007.